



Cite this: *Nanoscale Adv.*, 2025, **7**, 1077

## A new mesoporous Ce–Mn–LDH-based Co-MOF nano-composite for the green synthesis of tetrazoloquinazolines†

Samira Javadi and Davood Habibi \*

Tannic acid (TA), as a plant polyphenol, has many active sites for chelation with metals, so TA-oligomers (TA-Olig) were used for the first time as ligands on the surface of Ce–Mn–LDH to prepare the layered double hydroxide-based metal–organic framework (Ce–Mn–LDH@CPTMS@TA-Olig@Co-MOF = E) nanocomposite. In this regard, a homogeneous water/ethanol solution was prepared by sol–gel method using polyethylene glycol and ammonia solution, and then TA was converted into a set of oligomers in the presence of formaldehyde. In the next step, Ce–Mn–LDH was prepared in a ratio of 1 : 4 of Ce to Mn, modified with 3-chloropropylmethoxysilane, functionalized by TA-Olig, and then cobalt salt was used to prepare E. Finally, the structure of E was determined by FT-IR, ICP, XRD, BET, EDX, SEM, SEM-mapping, TEM, and TGA-DTA techniques and used as a new and potent nanocatalyst for the synthesis of tetrazoloquinazolines **a(1–12)**. One of the advantages of this nanocatalyst is the active surface to form products in a limited time in mild conditions with high efficiency and easy separation. Also, the catalytic activity is maintained even after four consecutive runs.

Received 1st August 2024  
Accepted 15th November 2024

DOI: 10.1039/d4na00643g  
[rsc.li/nanoscale-advances](http://rsc.li/nanoscale-advances)

## 1. Introduction

The spherical structure of colloidal particles, with diameters ranging from 0.01 to 1  $\mu\text{m}$ , has been extensively studied in fields such as catalysis, drug delivery, medicine, material science, and biology.<sup>1</sup>

Among the various approaches for preparing stable colloidal particles, the Stöber method has been developed. A key strategy in this method is the preparation of silica-containing colloidal particles using the sol–gel process, which creates a homogeneous system for colloidal particles with a uniform structure, facilitating the synthesis of various types of polymer and mineral spheres, such as resorcinol-formaldehyde spheres.<sup>2,3</sup> Coordination polymers (CPs) or metal–organic frameworks (MOFs) are networks composed of organic linkers and metal centers. They exhibit diverse structures and tunable particle sizes, which have attracted significant attention over the last two decades.<sup>4,5</sup>

Metal–phenol coordination polymers (MPCPs) are a subset of metal–organic coordination polymers that are typically prepared using plant polyphenols, such as TA, as organic ligands. The interaction between metal species and catechol groups facilitates their formation. Owing to their high surface

area, MPCPs find applications in biomedicine, sensors, and catalysis.<sup>6,7</sup> TA is a natural polyphenol from the phenolic acid group, consisting of a central glucose unit with ten gallic acid molecules attached to it.<sup>8,9</sup> A unique feature of TA is the strong interaction between catechol groups and metal ions, which leads to extensive chemical compatibility, especially in metal ion complexes.<sup>10</sup>

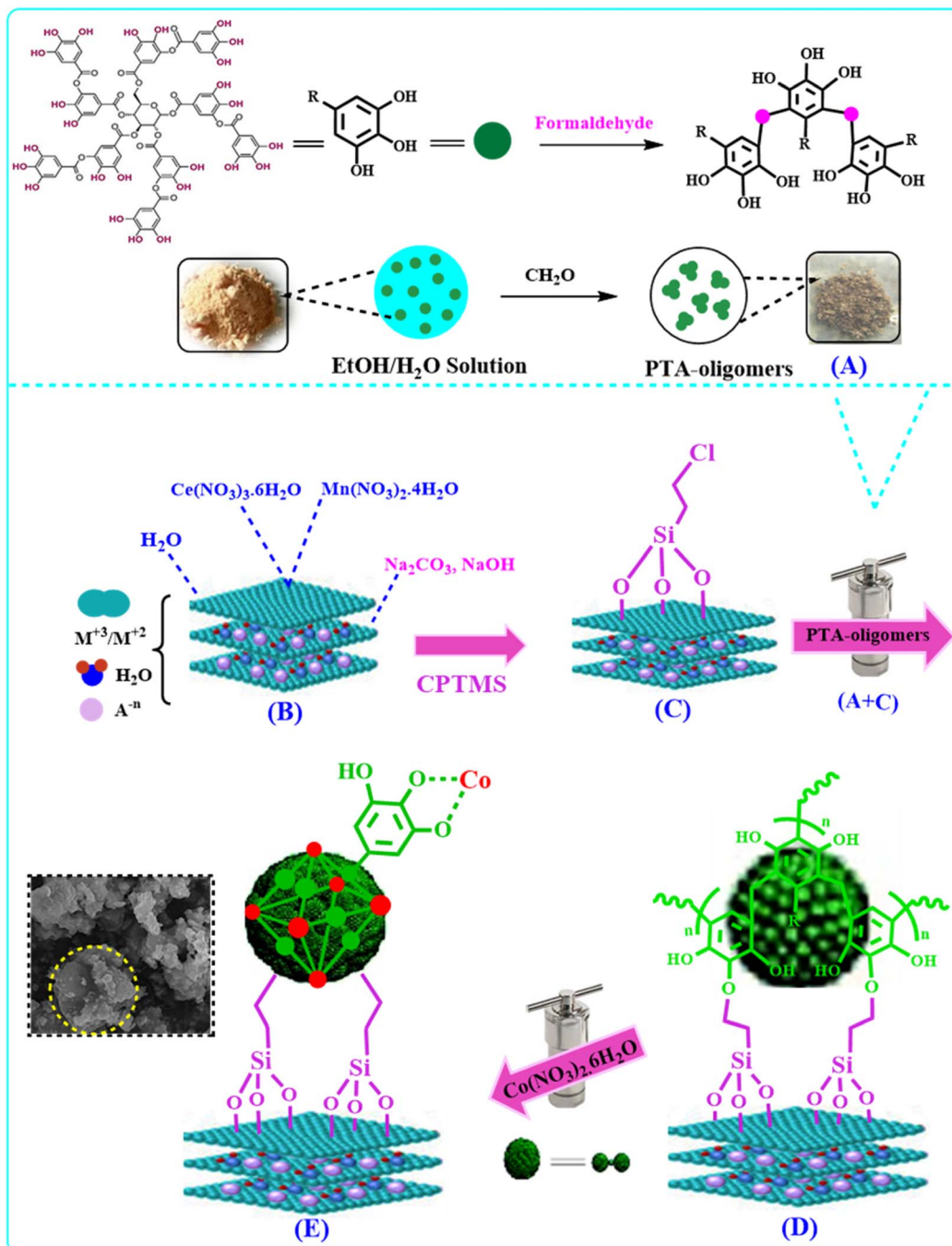
The design of nanoporous solid materials from two-dimensional materials, such as transition metal dichalcogenides (TMDs), layered double hydroxides (LDHs), graphene oxide, etc., has attracted much attention nowadays.<sup>11–13</sup> LDHs, or pseudo hydroxylite, are a group of two-dimensional layered solids in which divalent and trivalent metal cations, as well as interlayer anions, are present in their semi-hydrophilic structure.<sup>14</sup>

The integration of two MOF and LDH structures into a composite with unique properties is a smart design to increase the catalytic performance.<sup>15</sup> In this method, the uniform growth of MOF crystals on LDH plates results in the formation of organic–mineral hybrid materials with high porosity and surface area, which are used in the fields of catalysis, energy storage, absorption, and optoelectronics.<sup>16,17</sup> Therefore, synthesizing these composites *via* a simple, cost-effective, and environmentally friendly method is of great importance.<sup>18</sup> In most studies, these composites have been used as absorbers for the removal of metal pollutants from the environment due to their high porosity. In this work, we have utilized them as a green and powerful catalyst for the synthesis of quinazolines. For example, Soltani and colleagues, in 2021,

Department of Organic Chemistry, Faculty of Chemistry and Petroleum Sciences, Bu-Ali Sina University, Hamedan, Iran. E-mail: [davood.habibi@gmail.com](mailto:davood.habibi@gmail.com); [dhabibi@basu.ac.ir](mailto:dhabibi@basu.ac.ir); Fax: +98-81-31408025; Tel: +98-81-38380922

† Electronic supplementary information (ESI) available. See DOI: <https://doi.org/10.1039/d4na00643g>





Scheme 1 Synthesis of E.

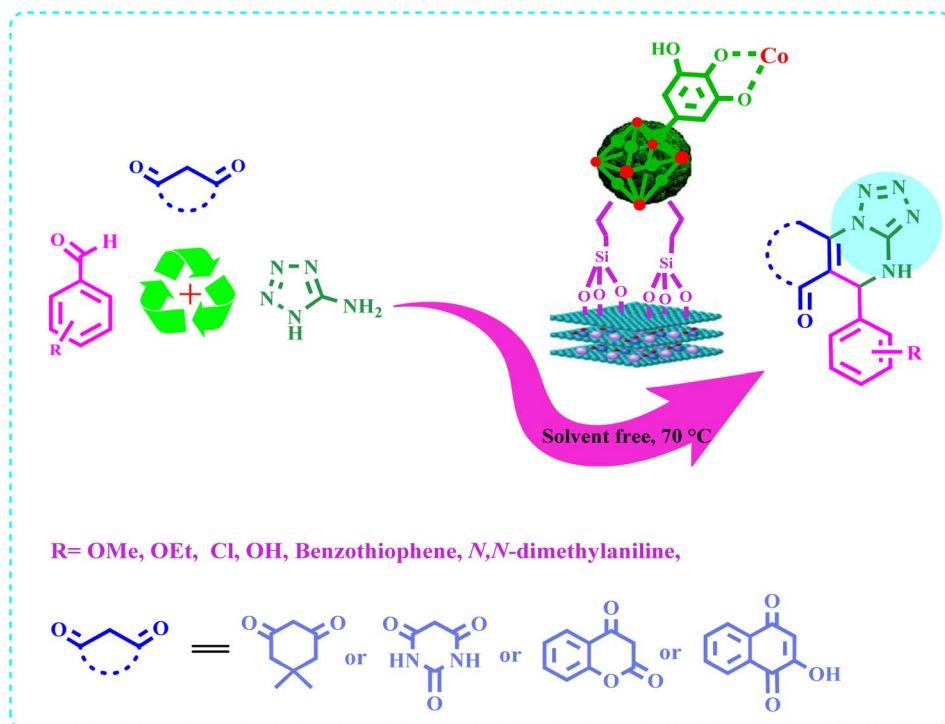
utilized MOF growth on NiCo-LDH to synthesize a NiCo-LDH/MOF nanocomposite for removing metal ions from an aqueous medium.<sup>19</sup> Mallakpour and colleagues modified the surface of LDH with chitosan and TA to absorb reactive dyes.<sup>20</sup>

Quinazolines are nitrogen-containing heterocycles that were prepared by Gabriel in 1903, with other names such as phenazine, 6-benzopyrimidine, and benzo-1,3-diazine also known. Quinazolines are nitrogen-containing cyclic heterocycles that were prepared by Gabriel in 1903, with other names such as phenazine, 6-benzopyrimidine, and benzo-1,3-diazine also

known.<sup>21</sup> Quinazolines and tetrazole-pyrimidines indeed have a wide field of biological activities,<sup>22,23</sup> and are known for their anti-cancer, anti-diabetic, anti-inflammatory, anti-microbial, anti-hypertensive, and anti-convulsant.<sup>24,25</sup> Therefore, the synthesis of tetrazole-pyrimidines was reported by  $\text{Ba}_{0.5}\text{Sr}_{0.5}\text{-Fe}_{12}\text{O}_{19}\text{@PU-SO}_3\text{H}$ ,<sup>26</sup>  $p\text{-TsOH}$ ,<sup>27</sup>  $\text{Fe}_3\text{O}_4\text{@C/Ph-SO}_3\text{H}$ ,<sup>28</sup>  $\text{TsOH}$ ,<sup>29</sup>  $\text{AlCl}_3$ ,<sup>30</sup> and  $\text{Fe}_3\text{O}_4\text{@PEG-400-SO}_3\text{H}$ .<sup>31</sup>

In this work, based on the principles of green chemistry, TA was used to prepare corresponding TA-Olig with abundant catechol groups to be chelated to metal to form a coordinated





Scheme 2 Synthesis of a(1-12).

metal-phenolic compound in an easy and green way. So, Ce-Mn-LDH was used as a scaffold for the preparation of the stable metal-phenolic coordinated compound (Scheme 1).

Finally, E was characterized by FT-IR, ICP, XRD, EDX, SEM, SEM-mapping, TEM, and TGA-DTA techniques and used as a potent nanocatalyst for the green synthesis of tetrazolo-[1,5-*a*] quinazolines **a(1-12)** from the three component condensation reaction of 5-amino-tetrazole, aldehydes, and diketones under solvent-free conditions at 70 °C with short reaction times and high yields (Scheme 2).

## 2. Experimental

### 2.1. Material

All chemicals [Ce(NO<sub>3</sub>)<sub>3</sub>·6H<sub>2</sub>O, Mn(NO<sub>3</sub>)<sub>2</sub>·4H<sub>2</sub>O, Co(NO<sub>3</sub>)<sub>2</sub>·6H<sub>2</sub>O, TA, Na<sub>2</sub>CO<sub>3</sub>, NaOH, toluene, and ethanol] were purchased from the Aldrich and Merck chemical companies and used as received.

### 2.2. Equipment

Melting points were determined by A BUCHI 510 device in open capillary tubes. FT-IR spectra were recorded on a PerkinElmer GX spectrophotometer using KBr. <sup>1</sup>H and <sup>13</sup>C NMR spectra were recorded on a BRUKER AVANCE 300 MHz instrument in DMSO-*d*<sub>6</sub>. Crystalline structures of products were identified on a Bruker D<sub>8</sub> Advance XRD instrument with Cu K $\alpha$  as the incident radiation ( $\lambda = 1/56\,054\text{ \AA}$ ) (40 kV and 100 mA). The catalyst particles' morphology was determined *via* the SEM images on a Philips XL-30 operated at 30 kV accelerating voltage. Qualitative detection of the Ce and Mn elements was performed by

EDX in an ESEM (SIGM, Germany) instrument. The structure morphologies of the catalyst particles were determined *via* the TEM images using an EM10C instrument with an accelerating voltage of 100 kV. TGA-DTA analysis was performed with a heating rate of 30 °C min<sup>-1</sup> over a temperature range of 25–1200 °C using the PerkinElmer Pyris Diamond apparatus. The BET-BJH analyses were performed by BELSORP MINI II. The ICP measurements were performed using a PerkinElmer 5300 DV ICP/OES. Progress of the reaction progress was monitored by TLC (silica gel SIL G/UV 254 plates), and ultrasonication was performed by ultrasonic device 2200 ETH SONICA.

### 2.3. Synthesis of E

E was synthesized as follows:

**2.3.1. Stage one: preparation of TA-Olig (A).** A homogeneous solution of polyethylene glycol (PEG-500, 2 mL) and ammonia (25%, 0.5 mL) in (H<sub>2</sub>O:EtOH 5:1) was prepared in 1 hour at room temperature. Then, TA (1 g) was added to the solution. After homogenization (about 30 min), a saturated solution of CH<sub>2</sub>O in water (0.3 mL) was added and stirred for 24 hours. Then, A was autoclaved for 24 at 120 °C, centrifuged, and dried at 80 °C.<sup>3</sup>

**2.3.2. Stage two: preparation of Ce-Mn-LDH (B).** Solution number one was prepared by dissolving Ce(NO<sub>3</sub>)<sub>3</sub>·6H<sub>2</sub>O (2.6 g, 7 mmol) and Mn(NO<sub>3</sub>)<sub>2</sub>·4H<sub>2</sub>O (7.02 g, 28 mmol) (molar ratio: 1:4) in water (50 mL). Solution number two was prepared by dissolving Na<sub>2</sub>CO<sub>3</sub> (10.6 g, 0.1 mol) and NaOH (4 g, 0.1 mol) (molar ratio: 1:1) in water (50 mL), heated at 60 °C for 24 h and added dropwise to solution number one until the pH of the new solution reached 10. Then, the prepared dark brown solid (B)



was separated, washed several times with water, and oven-dried at 80 °C.

**2.3.3. Stage three: preparation of Ce–Mn–LDH@CPTMS (C).** **B** (1.0 g) was dispersed in toluene (50 mL) with ultrasonication for 15 min and (3-chloro-propyl)trimethoxysilane (CPTMS) (11 mmol, 2.0 mL) was added dropwise and the mixture refluxed at 110 °C for 12 h. **C** was collected and washed with toluene and ethanol several times and dried at 80 °C.

**2.3.4. Stage four: preparation of Ce–Mn–LDH@CPTMS@TA–Olig (D).** **C** (1 g) was dispersed in the  $\text{H}_2\text{O} : \text{EtOH}$  (5 : 1) mixture by ultrasonication for about 10 min. **A** (0.5 g) was also dispersed in  $\text{H}_2\text{O} : \text{EtOH}$  (ratio 5 : 1) by ultrasonication for about 10 min, and was then added dropwise to **C**, refluxed at 110 °C for 48 h, and **D** separated by centrifugation and dried at 80 °C.

**2.3.5. Stage five: preparation of Ce–Mn–LDH@CPTMS@TA–Olig@Co (E).** **D** (1 g) was dispersed in  $\text{H}_2\text{O} : \text{EtOH}$  (5 : 1) by ultrasonication for 10 min and  $\text{Co}(\text{NO}_3)_2 \cdot 6\text{H}_2\text{O}$  (0.29 g, 5 mmol) was added. The mixture refluxed at 110 °C for 24 h, autoclaved at 120 °C for 24 h, and **E** was collected and washed with  $\text{H}_2\text{O}$ /EtOH several times and dried at 80 °C.

## 2.4. General procedure for the synthesis of a(1–12)

A mixture of 5-amino-tetrazole (85 mg, 1 mmol), aldehyde (1 mmol), 1,3-diketone (280 mg, 1 mmol), and **E** (10 mg) was stirred in solvent-free condition at 70 °C for the specified time. After completion of the reaction (TLC, *n*-hexane/acetone 5 : 3), the mixture was cooled to room temperature, and hot ethanol (5 mL) was added to dissolve products. **E** was easily separated from the ethanolic solution by centrifugation, the product was washed with ethanol (3 × 20 mL), dried under reduced pressure, and characterized by comparing their IR, NMR spectra, and melting points with authentic samples.<sup>26</sup>

## 3. Results and discussion

### 3.1. Characterization of the catalyst

**E** was characterized by Fourier-Transform Infrared (FT-IR), X-ray Diffraction (XRD), Energy Dispersive X-ray (EDX), EDX-Mapping, Scanning Electron Microscopy (SEM), Transmission Electron Microscopy (TEM), Thermo-Gravimetric-Differential Thermal Analysis (TGA-DTA), Brunauer–Emmett–Teller (BET)–Barrett–Joyner–Halenda (BJH) and Inductively Coupled Plasma–Optical Emission Spectroscopy (ICP–OES) techniques.

**3.1.1. Characterization by FT-IR.** Fig. 1 shows the FT-IR spectra of TA and TA-Olig. In curve A, new peaks at 806, 611, 1104, and 1614  $\text{cm}^{-1}$  confirm the synthesis of TA-Olig.

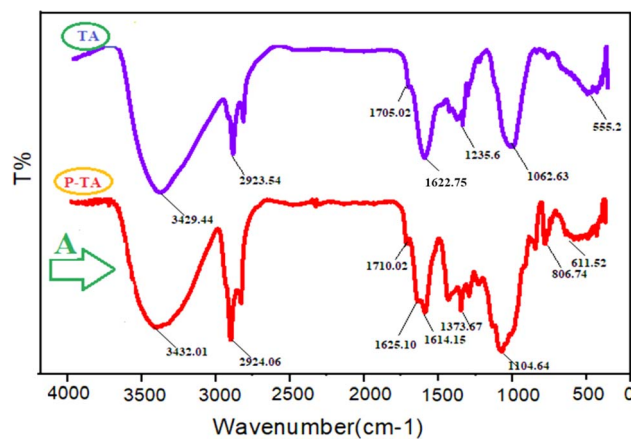


Fig. 1 Comparison of the FT-IR spectra of TA, and A.

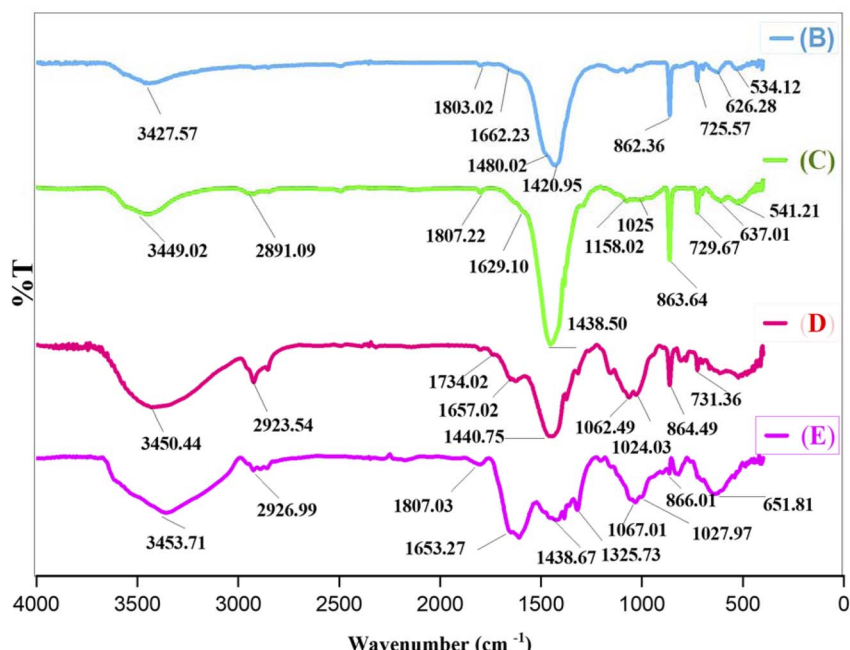


Fig. 2 Comparison of the FT-IR spectra of B, C, D, and E.



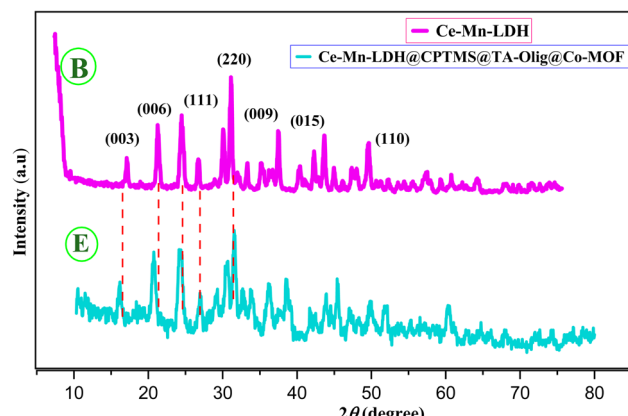


Fig. 3 The XRD patterns of B and E.

Fig. 2 represents the FT-IR spectra of **B**, **C**, **D**, and **E**.

Curve **B** exhibits three peaks at 626, 534, and 862  $\text{cm}^{-1}$ , corresponding to Ce–O, Mn–O, and Ce–O–Mn bonds,

respectively. The broad peak at about 3427  $\text{cm}^{-1}$  is attributed to the OH stretching vibrations, and the peak at 1662  $\text{cm}^{-1}$  is associated with the bending vibrations of interlayer water. Additionally, the peaks at 1803 and 1480  $\text{cm}^{-1}$  are linked to stretching and asymmetric vibrations of C–O and C=O bonds, respectively.

Curve **C** shows peaks at 1025 and 1158  $\text{cm}^{-1}$ , indicative of Si–O–M and Si–O–Si bonds.

In curve **D**, the shift of peaks to 1657 and 1734  $\text{cm}^{-1}$ , as well as the broadening of the peak at 3449  $\text{cm}^{-1}$ , indicates the functionalization of C with **A**.

In curve **E**, the presence of a Co–O peak at about 651  $\text{cm}^{-1}$ , confirms the successful synthesis of **E**.

**3.1.2. Characterization by XRD.** The XRD structural information of **B** and **E** is depicted in Fig. 3. The sharp and symmetrical peaks indicate the structural specifications of hydrotalcite. There are diffraction peaks at  $2\theta = 15.85^\circ$ ,  $24.1^\circ$ ,  $26.45^\circ$ ,  $31.3^\circ$ ,  $44.95^\circ$ ,  $51.55^\circ$ , and  $52^\circ$ , corresponding to the (003), (006), (111), (220), (009), (015), and (110) crystal planes of

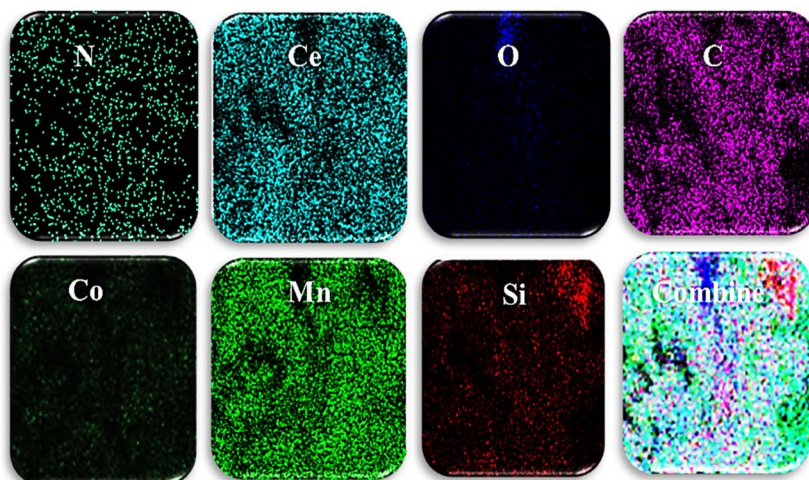
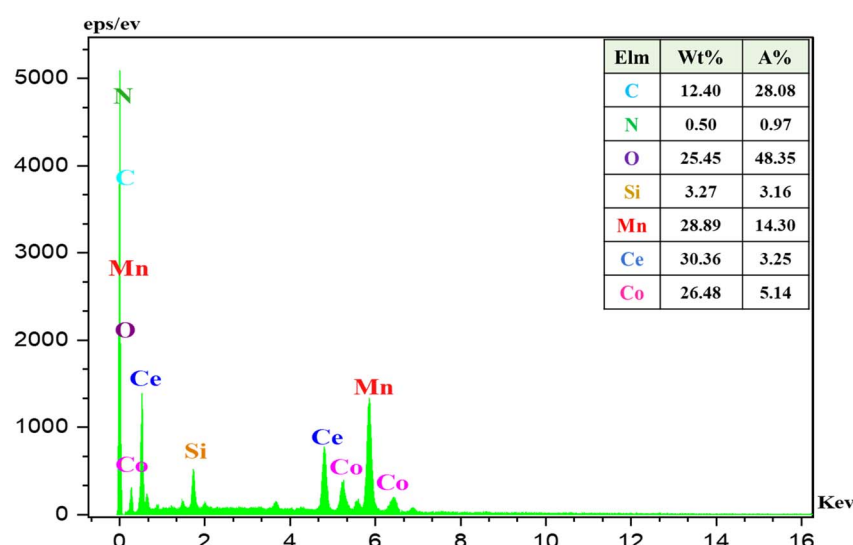


Fig. 4 The FESEM-EDX-mapping images of E.



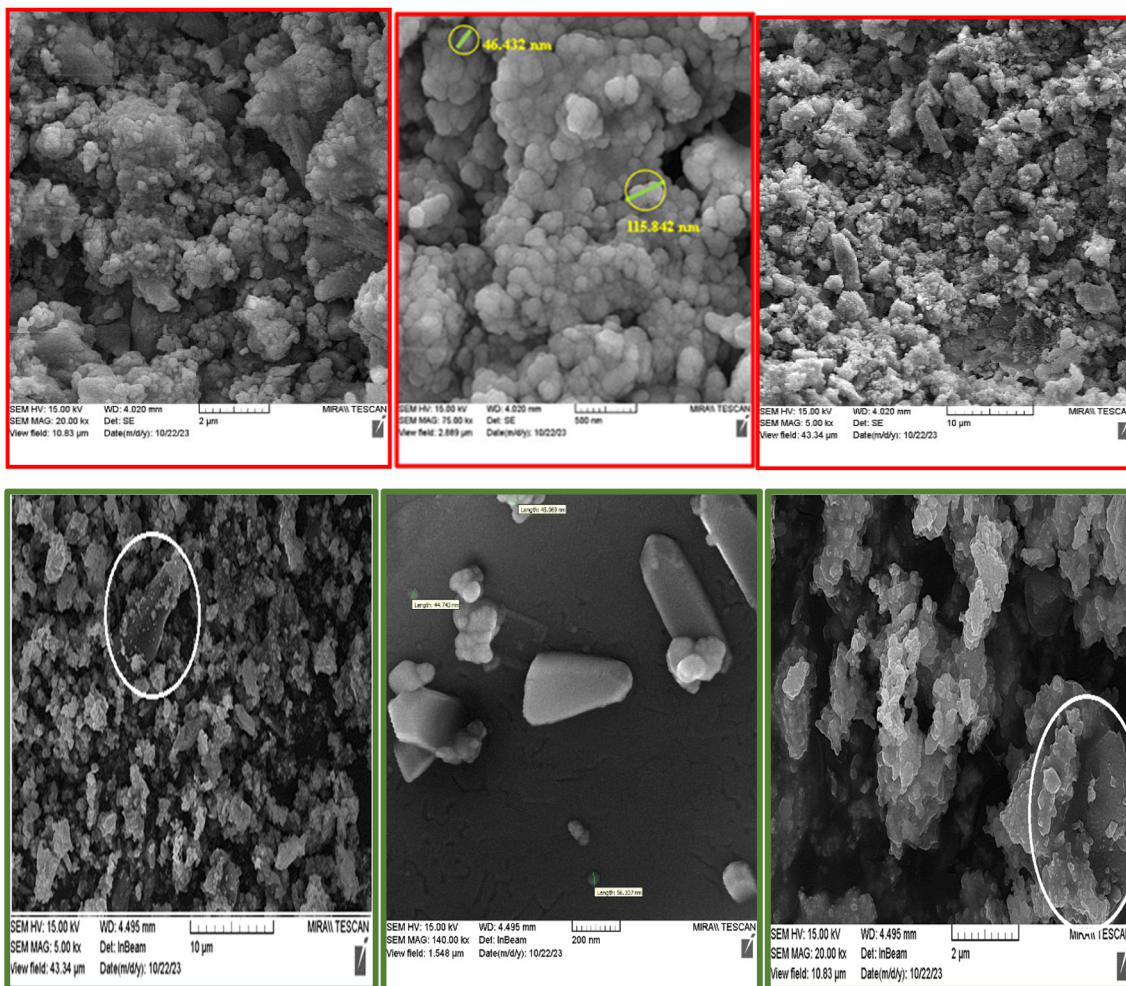


Fig. 5 The SEM images of A and E.

B. The (003) peak shows the degree of crystallinity of structure and the success of B.<sup>32-35</sup>

In graph E, the peak intensities are diminished, and the emergence of peaks at around 41.5°, 44.2°, and 47.3° shows the formation of Co-MOF (Co-PTA). The XRD pattern of the E composite indicates the simultaneous presence of both B and E in the composite structure and the growth of Co-MOF (Co-PTA) crystals on the Ce-Mn-LDH sheets.<sup>36</sup>

**3.1.3. Characterization by FESEM-EDX-mapping.** The SEM-EDX mapping of E and the corresponding structural elements are shown in Fig. 4. EDX content analysis confirms the presence of Ce, Mn, O, N, Co, Si, and C elements and FESEM-mapping shows that the LDH/MOF has a uniform surface structure with a homogeneous distribution of these elements. It means that the Co-MOF (Co-PTA) nanocrystals are uniformly distributed on the LDH ultrathin sheets.

**3.1.4. Characterization by the SEM images.** The morphology of A and E was confirmed by the SEM images as shown in Fig. 5 (first row). The spherical morphology suggests that the polymerization process was controlled and consistent, and the spherical shape and the average particle size are estimated to be in the nanometer range (86–115 nm), which is

a confirmation of the polymerization of TA. Nano-particles can sometimes aggregate, forming larger clusters or blocks, which can occur during sample preparation or due to interactions between the nanoparticles and the LDH sheets.

The FESEM images (Fig. 5, second row) clearly show the presence and successful growth of Co-MOF (Co-PTA) nanoparticles on surface of the Ce-Mn-LDH ultrathin nanosheets.

**3.1.5. Characterization by the TEM images.** The crystalline structure and morphology of Ce-Mn-LDH@CPTMS@TA-Olig@Co-MOF were studied by the TEM images (Fig. 6). Accordingly, the core–shell structure and the arrangement of metal spheres Co-MOF (Co-PTA) on the Ce-Mn-LDH sheets are visible.

**3.1.6. Characterization by TGA-DTA.** The thermal behavior of E was determined by the TGA-DTA curves in the temperature range of 25 to 1000 °C. The gradual weight loss of the catalyst starts at about 75 °C and continues until about 700 °C. This gradual decrease in catalyst weight at around 75 °C can be attributed to the removal of molecules that do not have a strong bond with the main skeleton of the catalyst, or possibly the start of removal of water molecules. The weight loss at about 266 to 400 °C is related to the decomposition of the organic part of the

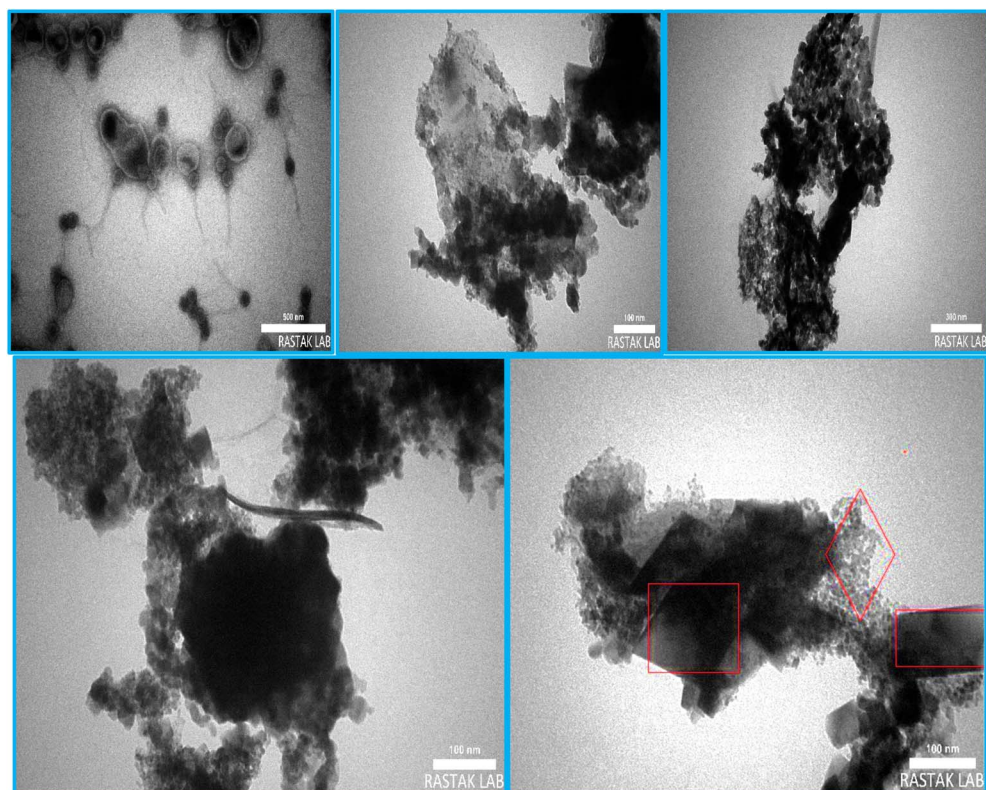


Fig. 6 The TEM images of E.

composite (probably water molecules and organic solvents trapped in the pores and cavities of the catalyst). From 400 to 700 °C, with continuous loss of weight (7% weight), the thermal decomposition of different parts of E occurs (Fig. 7).

**3.1.7. Characterization by BET/BJH.** The textural properties of B and E were evaluated through the nitrogen absorption and desorption analyzes (surface area, pore volume, and pore diameter). As shown in Table 1 and Fig. 8, the surface area

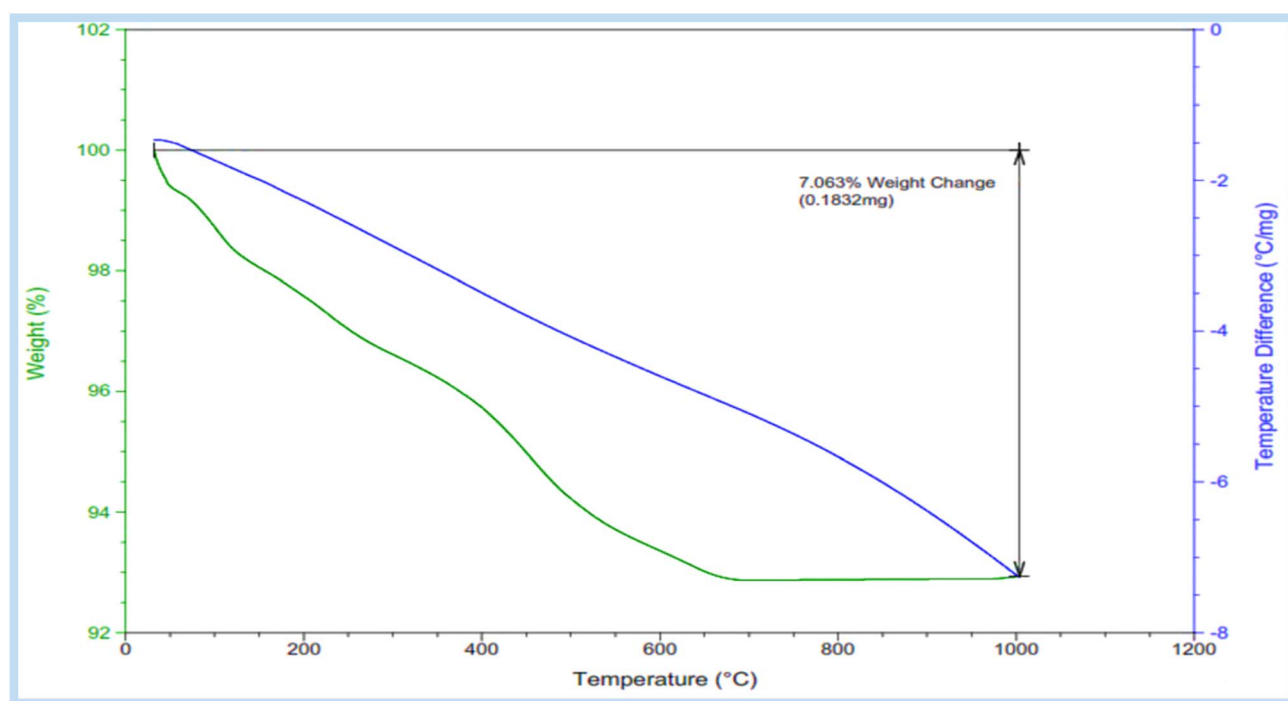


Fig. 7 The TGA-DTA curve of E.



Table 1 The  $N_2$  absorption–desorption parameters for B and E

	$S_{\text{BET}}$ ( $\text{m}^2 \text{ g}^{-1}$ )	$V_t$ ( $\text{cm}^3 \text{ g}^{-1}$ )	$D_{\text{BJH}}$ (nm)
B	27.833	0.1899	27.296
E	20.878	0.0701	13.445

decreases from **B** ( $27.833 \text{ m}^2 \text{ g}^{-1}$ ) to **E** ( $20.878 \text{ m}^2 \text{ g}^{-1}$ ), indicating that the growth of Co-MOF (Co-PTA) crystals on the surface of **B** has been carried out, leading to a decrease in the available surface in **E**.

The significant decrease in pore volume from **B** ( $0.1899 \text{ cm}^3 \text{ g}^{-1}$ ) to **E** ( $0.0701 \text{ cm}^3 \text{ g}^{-1}$ ), indicates that the pores in **B** are being filled or blocked by the MOF crystals, which is consistent with the successful synthesis of **E**.

The decrease in pore diameter in **E** (13.445 nm) compared to **B** indicates the formation of Co-MOF (Co-PTA) crystals in the pores of **B** (27.296 nm), leading to smaller pore sizes.

The **E** isotherm shows some mesoporosity (pores with diameters between 2 and 50 nm), which is typical for materials with MOF structures. This porosity is probably due to the presence of MOF crystals, which create smaller and more uniform pores.

The **B** isotherm shows the absence of mesoporosity in **B**, the pores being larger and more irregular, which is consistent with the observed larger pore diameter.

**3.1.8. Characterization by ICP-OES.** The ICP analysis was used for measuring the amount of Co in **E** which was about  $30.54 \text{ mmol g}^{-1}$ .

### 3.2. Optimization

To optimize the synthesis of **10a**, the one-pot condensation reaction of 5-amino-tetrazole, 4-chlorobenzaldehyde, and dimedone was carried out in various temperatures, catalyst amounts, and solvents in the presence of **E**. The best optimal conditions were about 1:1:1 mole of 5-aminotetrazole, 4-chlorobenzaldehyde, and dimedone with 10 mg of **E** at  $70^\circ\text{C}$  under solvent-free conditions (Table 2).

### 3.3. Synthesis of a(1–12)

Based on the obtained results from the model reaction (1:1:1 molar ratio of 5-amino-tetrazole, 4-chlorobenzaldehyde, and dimedone, in ethanol with 10 mg of **E** at  $70^\circ\text{C}$ ), all synthesized compounds were characterized and approved with comparison of their spectroscopic data and melting points with authentic samples (Table 3).

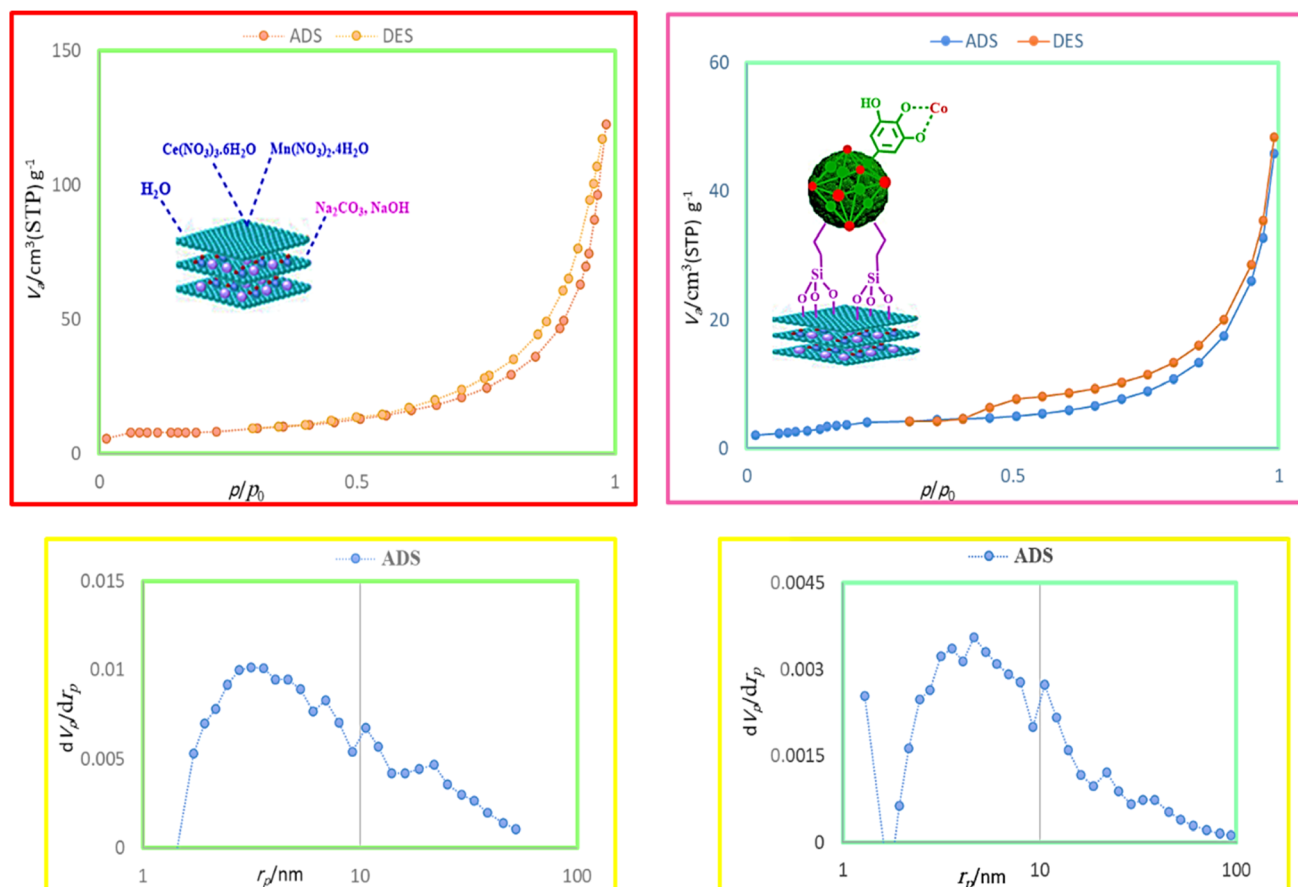


Fig. 8 The BET and BJH analyses of B and E.



Table 2 Optimization of the reaction conditions for preparation of 10a by E<sup>a</sup>

Entry	Amount of catalyst	Solvent	Temp (°C)	Time (min)	Yield <sup>b</sup> (%)
1	10 mg	EtOH	r.t.	45	70
2	10 mg	CHCl <sub>3</sub>	r.t.	60	40
3	10 mg	CH <sub>2</sub> Cl <sub>2</sub>	r.t.	80	35
4	10 mg	CH <sub>3</sub> CN	r.t.	70	54
5	10 mg	Solvent-free	r.t.	30	50
6	10 mg	EtOH	Reflux	20	80
7	10 mg	CHCl <sub>3</sub>	Reflux	60	68
8	10 mg	CH <sub>2</sub> Cl <sub>2</sub>	Reflux	70	58
9	10 mg	CH <sub>3</sub> CN	Reflux	25	80
10	10 mg	Solvent-free	60	20	85
11	<b>10 mg</b>	<b>Solvent-free</b>	<b>70</b>	<b>5</b>	<b>90</b>
12	10 mg	Solvent-free	80	10	88
13	10 mg	Solvent-free	90	10	88
14	20 mg	Solvent-free	70	30	71
15	30 mg	Solvent-free	70	25	77
16	No catalyst	Solvent-free	70	120	65

<sup>a</sup> Conditions: 5-aminotetrazol (1 mmol), 4-chlorobenzaldehyde (1 mmol), dimedone (1 mmol), solvent-free. <sup>b</sup> Isolated pure yield.

### 3.4. Spectral data of a(1–12)

**3.4.1. 5-(2-Methoxyphenyl)-4,5-dihydrobenzo[*g*]tetrazolo[1,5-*a*]quinazoline-6,11-dione (1a).**<sup>27</sup> Yield: 78%, m.p. 278–281 °C; IR:  $\nu$  = 3233.50, 3086, 2928, 1665.66, 1643.82, 1618.56, 1586.63, 1525.10, 1344.61, 1303.11, 1199.80, 724.82  $\text{cm}^{-1}$ . <sup>1</sup>H NMR (300 MHz, DMSO-*d*<sub>6</sub>)  $\delta$ <sub>H</sub> = 12.04 (s, 1 NH), 8.08–7.58 (s, ArH), 7.55–7.08 (d, *J* = 7.6 Hz, 2 ArH), 6.94 (d, *J* = 8.0 Hz, 2 ArH), 3.62 (s, 1H, MeOH) ppm. <sup>13</sup>C NMR (75 MHz, DMSO-*d*<sub>6</sub>)  $\delta$ <sub>C</sub> = 149.70, 139.71, 135.57, 134.38, 131.99, 130.89, 126.66, 126.38, 120.84, 115.10, 112.83, 112.37, 56.13, 40.97, 40.63, 40.30, 39.97, 39.63, 39.30, 38.96 ppm.

**3.4.2. 5-(4-(Dimethylamino)phenyl)-4,5-dihydrobenzo[*g*]tetrazolo[1,5-*a*]quinazoline-6,11-dione (2a).**<sup>27</sup> Yield: 88%, m.p. 333–335 °C; IR:  $\nu$  = 3424.50, 292.81, 1682.09, 1580.12, 1574.06, 130.76, 1259.89, 1022.70, 754  $\text{cm}^{-1}$ . <sup>1</sup>H NMR (300 MHz, DMSO-*d*<sub>6</sub>)  $\delta$ <sub>H</sub> = 12.05 (s, 1 NH), 8.45–7.56 (d, *J* = 8.8 Hz, 2 ArH), 7.28–6.94 (d, *J* = 7.6 Hz, 2 ArH), 5.18 (s, Hz, ArH), 3.62 and 3.52 (s, 2 CH<sub>3</sub>) ppm. <sup>13</sup>C NMR (75 MHz, DMSO-*d*<sub>6</sub>)  $\delta$ <sub>C</sub> = 180.45, 179.01, 157.63, 135.56, 135.33, 134.13, 132.54, 131.95, 131.40, 130.82, 126.93, 126.67, 126.15, 125.44, 120.85, 120.69, 112.52, 112.36, 56.10, 55.22, 40.94, 40.61, 40.28, 39.94, 39.61, 39.28, 38.95 ppm.

**3.4.3. 5-(Thiophen-2-yl)-4,5-dihydrobenzo[*g*]tetrazolo[1,5-*a*]quinazoline-6,11-dione (3a).**<sup>37</sup> Yield: 80%, m.p. 302–304 °C; IR:  $\nu$  = 338.95, 2923.78, 1682.25, 1597.91, 1573.82, 1375, 1061.7, 474  $\text{cm}^{-1}$ . <sup>1</sup>H NMR (300 MHz, DMSO-*d*<sub>6</sub>)  $\delta$ <sub>H</sub> = 14.47 (s, 1 NH), 7.91–7.06 (d, *J* = 8.4 Hz, 2 ArH), 6.30 (d, *J* = 6.8 Hz, 2 ArH), 5.54 (s, ArH) ppm. <sup>13</sup>C NMR (75 MHz, DMSO-*d*<sub>6</sub>)  $\delta$ <sub>C</sub> = 178.61, 172.55, 151.46, 149.99, 144.49, 139.63, 137.03, 134.87, 133.19, 128.64, 126.08, 124.56, 122.80, 121.49, 120.74, 41.30, 21.18 ppm.

**3.4.4. 5-(4-Nitrophenyl)-4,5-dihydro-6*H*-chromeno[3,4-*e*]tetrazolo[1,5-*a*]pyrimidin-6-one (4a).**<sup>38</sup> Yield: 90%, m.p. 265–270 °C; IR:  $\nu$  = 3419.5, 3255.67, 3074.36, 2923, 2727, 1666.23, 1614.88, 1563.77, 1523.48, 1491.60, 1453.91, 1313.33, 1266.27, 1215.92, 856.15, 785.94, 682.58  $\text{cm}^{-1}$ . <sup>1</sup>H NMR (300 MHz, DMSO-*d*<sub>6</sub>)  $\delta$ <sub>H</sub> = 10.14 (s, 1 NH), 8.37 (s, ArH), 8.05 (d, *J* = 7.6 Hz,

2 ArH), 7.84 (d, *J* = 8.4 Hz, 2 ArH), 7.55 (m, 2 ArH), 7.38–7.30 (d, *J* = 8.8 Hz, 2 ArH), 6.38 (s, ArH) ppm. <sup>13</sup>C NMR (75 MHz, DMSO-*d*<sub>6</sub>)  $\delta$ <sub>C</sub> = 192.74, 167.15, 164.87, 152.88, 132.11, 124.51, 123.87, 123.62, 116.26, 103.64, 40.55, 40.24, 39.90, 39.57, 39.23 ppm.

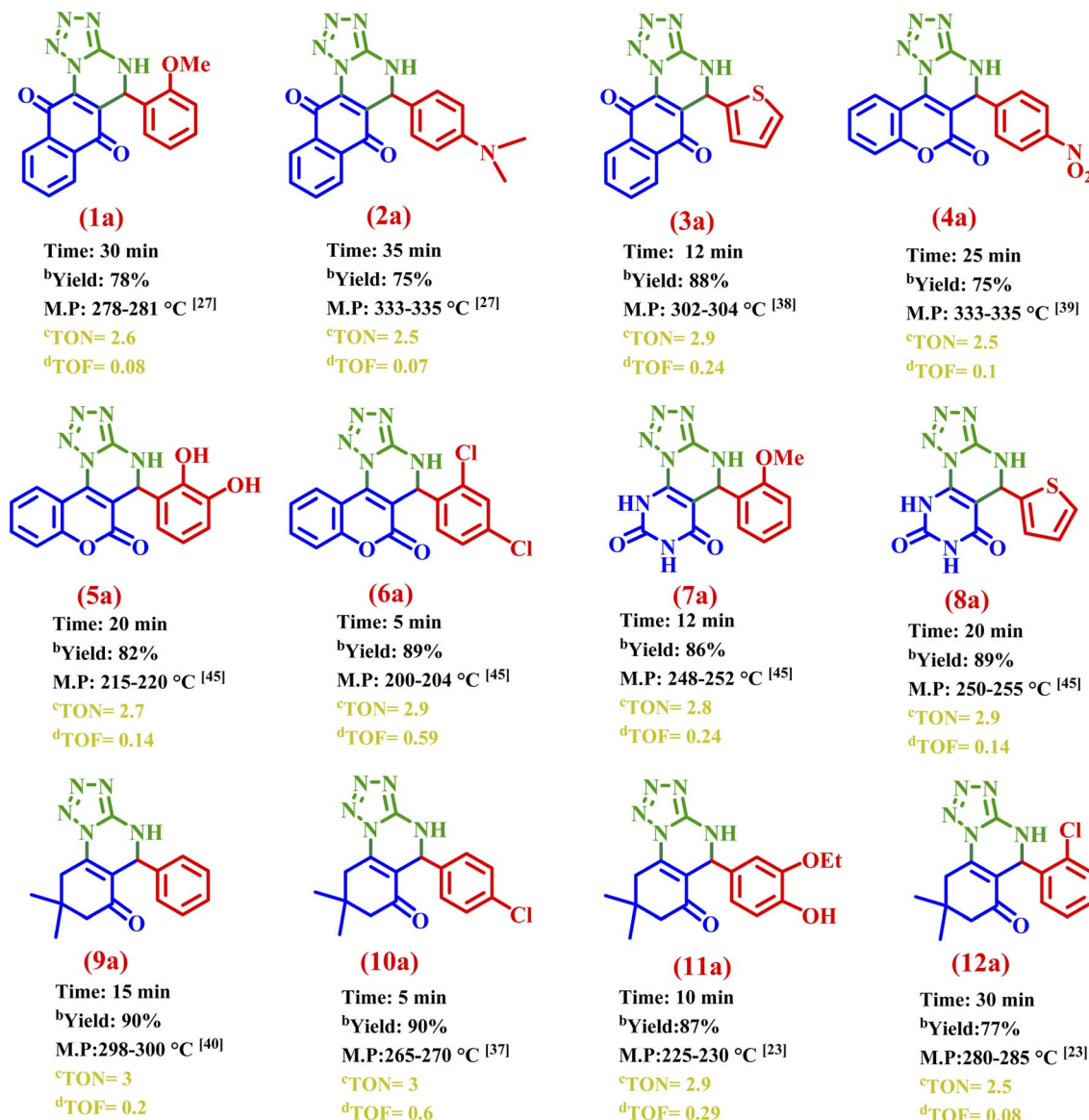
**3.4.5. 5-(2,3-Dihydroxyphenyl)-4,5-dihydro-6*H*-chromeno[3,4-*e*]tetrazolo[1,5-*a*]pyrimidin-6-one (5a).**<sup>39</sup> Yield: 82%, m.p. 215–220 °C; IR:  $\nu$  = 3429.7, 3213.65, 3087.89, 2850.86, 1755.73, 1703.58, 1574.94, 1443.59, 1413.96, 1289.40, 1202.39, 1093.16, 1019.75, 989.51, 838.75, 717.50  $\text{cm}^{-1}$ . <sup>1</sup>H NMR (300 MHz, DMSO-*d*<sub>6</sub>)  $\delta$ <sub>H</sub> = 12.15 (s, 1 OH), 9.84 (s, 1 NH), 8.31–8.01 (s, ArH), 7.65–7.43 (d, *J* = 8.2 Hz, 2 ArH), 6.92–5.69 (d, *J* = 8.4 Hz, 2 ArH), 3.46 (s, 1 OH) ppm. <sup>13</sup>C NMR (75 MHz, DMSO-*d*<sub>6</sub>)  $\delta$ <sub>C</sub> = 183.80, 159.64, 149.64, 143.01, 129.08, 128.03, 127.26, 124.59, 119.59, 118.12, 116.13, 114.29, 40.89, 40.56, 40.23, 39.89, 39.56, 39.22, 38.89 ppm.

**3.4.6. 5-(2,4-Dichlorophenyl)-4,5-dihydro-6*H*-chromeno[3,4-*e*]tetrazolo[1,5-*a*]pyrimidin-6-one (6a).**<sup>39</sup> Yield: 89%, m.p. 200–204 °C; IR:  $\nu$  = 3417.89, 3332.30, 3216.45, 1674.38, 1651.74, 1589.22, 1454.06, 1374.95, 1265.15, 1143.66, 1049.65, 1000.03, 736.16, 679.84  $\text{cm}^{-1}$ . <sup>1</sup>H NMR (300 MHz, DMSO-*d*<sub>6</sub>)  $\delta$ <sub>H</sub> = 11.02 (s, 1 NH), 7.64 (s, ArH), 7.59–7.34 (d, *J* = 7.4 Hz, 2 ArH), 7.07–7.01 (d, *J* = 7.8 Hz, 2 ArH), 6.94–6.84 (m, 2 ArH) ppm. <sup>13</sup>C NMR (75 MHz, DMSO-*d*<sub>6</sub>)  $\delta$ <sub>C</sub> = 184.83, 159.80, 151.16, 138.80, 125.11, 123.19, 118.24, 116.31, 112.64, 40.93, 40.60, 40.27, 39.94, 39.60, 39.27, 38.94 ppm.

**3.4.7. 5-(Thiophen-2-yl)-5,9-dihydropyrimido[5,4-*e*]tetrazolo[1,5-*a*]pyrimidine-6,8(4*H*,7*H*)-dione (7a).**<sup>39</sup> Yield: 89%, m.p. 250–255 °C; IR:  $\nu$  = 3424.60, 3202.39, 3086, 2846.70, 1735.27, 1676.74, 1598.43, 1555.99, 1440.71, 1306.36, 1251.44, 1203.68, 1166.33, 1016.03, 795.43, 758.81  $\text{cm}^{-1}$ . <sup>1</sup>H NMR (300 MHz, DMSO-*d*<sub>6</sub>)  $\delta$ <sub>H</sub> = 11.30 (s, 1 NH), 11.26 (s, 1 NH), 8.55–8.14 (s, ArH), 7.33 (s, 1 NH), 3.45, 2.48. <sup>13</sup>C NMR (75 MHz, DMSO-*d*<sub>6</sub>)  $\delta$ <sub>C</sub> = 183.78, 159.60, 149.65, 137.70, 132.21, 127.25, 124.56, 119.56, 114.27, 40.93, 40.61, 40.27, 39.94, 39.60, 39.27 ppm.

**3.4.8. 5-(2-Methoxyphenyl)-5,9-dihydropyrimido[5,4-*e*]tetrazolo[1,5-*a*]pyrimidine-6,8(4*H*,7*H*)-dione (8a).**<sup>39</sup> Yield: 86%,



Table 3 Synthesis of **a(1–12)** by **E**<sup>a</sup>

<sup>a</sup> Reaction conditions: 5-amino tetrazole (1 mmol), 4-chloroaldehyde (1 mmol), dimedone (1 mmol), **E** (10 mg) in solvent-free condition, at 70 °C.

<sup>b</sup> Isolated yield. <sup>c</sup> TON (turnover number): based on the ICP measurements at a ratio of 1 : 4, the content of Co in the catalyst is about 30.54, so the mmole of Co in 10 mg of the catalyst is 0.3 mmole g<sup>-1</sup>. For entry 1, since the yield is about 78%, the effective mmole the TON is 0.78 ÷ 0.3 = 2.6.

<sup>d</sup> TOF (turnover frequency): TOF = TON ÷ time. For entry 1, since the time is about 30 min, the TOF is 2.6 ÷ 30 = 0.08.

m.p. 248–252 °C; IR:  $\nu$  = 3427.20, 3203.10, 3152.20, 3054.55, 2853.10, 1751.15, 1696.89, 1654.66, 1549.88, 1395.94, 1233.70, 1062.40, 860.16 cm<sup>-1</sup>. <sup>1</sup>H NMR (300 MHz, DMSO-*d*<sub>6</sub>)  $\delta$ <sub>H</sub> = 11.34 (s, 1 NH), 11.15 (s, 1 NH), 8.48–7.49 (s, ArH), 7.46–6.99 (d, *J* = 7.6 Hz, 2 ArH), 6.96 (d, *J* = 7.8 Hz, 2 ArH), 6.93 (s, 1 NH), 3.86 (s, 1H, MeOH) ppm. <sup>13</sup>C NMR (75 MHz, DMSO-*d*<sub>6</sub>)  $\delta$ <sub>C</sub> = 163.88, 161.91, 159.46, 150.34, 134.57, 132.91, 121.94, 119.92, 111.41, 56.34, 40.58, 40.25, 39.91, 39.58, 39.25, 38.92 ppm.

**3.4.9. 8,8-Dimethyl-5-phenyl-5,7,8,9-tetrahydrotetrazolo[1,5-*a*]quinazolin-6(4*H*)-one (9a).**<sup>40</sup> Yield: 90%, m.p. 298–300 °C; IR:  $\nu$  = 3429.7, 3241.3, 3170.88, 3062.29, 2933.67, 1651.97, 1580.85, 1552.45, 1422.70, 1457.27, 1367.34, 1325.52, 1225.25,

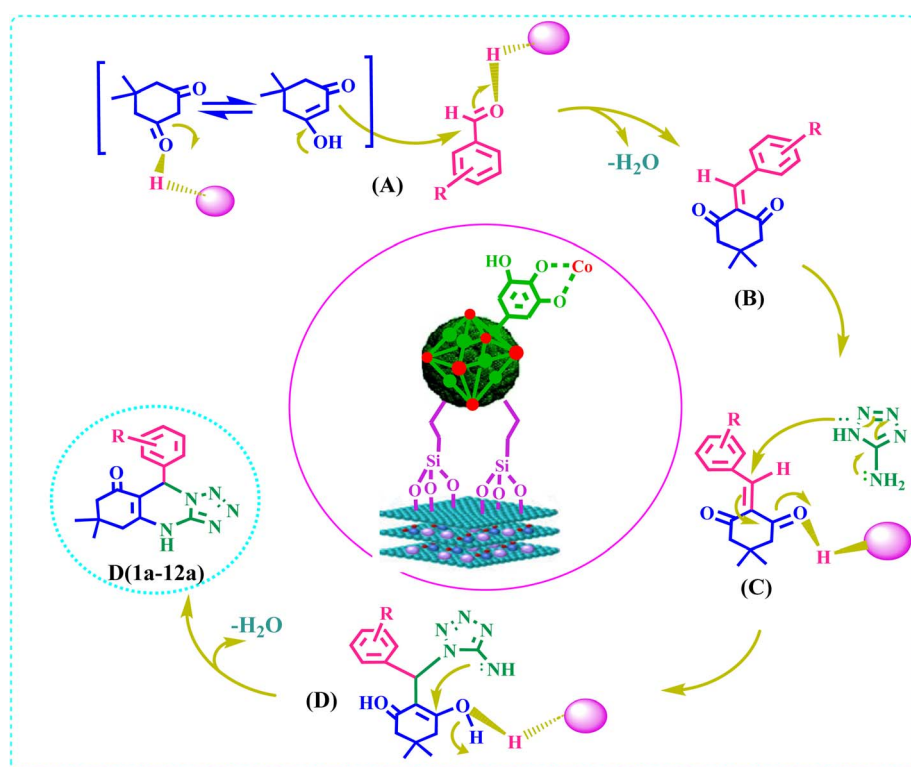
986.95, 843.23, 734.72 cm<sup>-1</sup>. <sup>1</sup>H NMR (300 MHz, DMSO-*d*<sub>6</sub>)  $\delta$ <sub>H</sub> = 11.59 (s, 1 NH), 7.34–7.28 (m, 5 ArH), 6.70 (s, 9-CH), 2.58 (s, CH<sub>2</sub>), 2.14 (m, CH<sub>2</sub>), 2.08, and 0.98 (s, 2 CH<sub>3</sub>) ppm. <sup>13</sup>C NMR (75 MHz, DMSO-*d*<sub>6</sub>)  $\delta$ <sub>C</sub> = 193.46, 150.93, 148.91, 140.90, 137.57, 129.03, 127.60, 106.11, 57.89, 50.25, 40.63, 40.31, 39.97, 39.64, 39.31, 32.74, 28.70, 27.44 ppm.

**3.4.10. 5-(4-Chlorophenyl)-8,8-dimethyl-5,7,8,9-tetrahydrotetrazolo[1,5-*a*]quinazolin-6(4*H*)-one (10a).**<sup>41</sup> Yield: 90%, m.p. 265–270 °C; IR:  $\nu$  = 3434.80, 3246.40, 3177.70, 3057.58, 2960.84, 1652.58, 1584.56, 1468.23, 1430.71, 1369.54, 1338.26, 1228.17, 1051.61, 985.62, 847.08, 759.73, 562.77 cm<sup>-1</sup>. <sup>1</sup>H NMR (300 MHz, DMSO-*d*<sub>6</sub>)  $\delta$ <sub>H</sub> = 11.67 (s, 1 NH), 7.43 (d, *J* = 7.8 Hz, 2



Table 4 Comparison of E with other catalysts for the synthesis of a(1–12)

Entry	Catalyst	Conditions	Time (min)	Yield (%)	Ref.
1	<i>p</i> -TSOH	Solvent-free, 120 °C	2 h	84	26
2	Fe <sub>3</sub> O <sub>4</sub> @C/Ph SO <sub>3</sub> H	H <sub>2</sub> O, 80 °C	1 h	96	27
3	g-C <sub>3</sub> N <sub>4</sub> /NHSO <sub>3</sub> H	i-PrOH, 80 °C	4 h	95	28
4	NaN <sub>3</sub> , Hg(OAc) <sub>2</sub>	HOAc, 100 °C	6 h	67	29
5	AlCl <sub>3</sub>	CH <sub>3</sub> CN, reflux	3 h	92	30
6	I <sub>2</sub>	i-PrOH, reflux	10 min	92	42
7	<i>p</i> -TSA	Solvent-free, 70 °C	6 min	88	43
8	MNPs@SiO <sub>2</sub> -Pr ANDSA	EtOH/H <sub>2</sub> O, 100 °C	5 min	94	44
9	PyTFA	μW, 90 °C	25 min	93	45
10	Our catalyst	Solvent-free, 70 °C	5 min	90	This work



Scheme 3 Proposed mechanism for the synthesis of a(1–12).

ArH), 7.41–7.28 (d,  $J = 7.8$  Hz, 2 ArH), 6.89 (s, 9-CH), 2.57–2.06 (m, CH<sub>2</sub>), 1.05, and 1.00 (s, 2 CH<sub>3</sub>) ppm. <sup>13</sup>C NMR (75 MHz, DMSO-*d*<sub>6</sub>) δ<sub>C</sub> = 193.41, 151.61, 149.01, 137.39, 130.56, 127.90, 105.05, 56.27, 50.24, 40.95, 40.62, 39.61, 39.28, 38.95, 28.70, 27.93 ppm.

**3.4.11. 5-(3-Ethoxy-4-hydroxyphenyl)-8,8-dimethyl-5,7,8,9-tetrahydrotetrazolo[1,5-*a*]quin-azolin-6(4*H*)-one (11a).**<sup>23</sup> Yield: 87%, m.p. 225–230 °C; IR:  $\nu$  = 3429.70, 3238.80, 3172.60, 3060.50, 2968.10, 1651.91, 1580.88, 1422.65, 1367.40, 1315.59, 1245.53, 1140.89, 734.64, 702.79 cm<sup>-1</sup>.

**3.4.12. 5-(2-Chlorophenyl)-8,8-dimethyl-5,7,8,9-tetrahydrotetrazolo[1,5-*a*]quinazolin-6(4*H*)-one (12a).**<sup>23</sup> Yield: 77%, m.p. 280–285 °C; IR:  $\nu$  = 3456.20, 3209.80, 3154.85, 3064.27, 2959.18, 1634.51, 1562.41, 1491.80, 1417.98, 1304.19, 1235.80, 1139.40, 971.52, 804.29, 697.30 cm<sup>-1</sup>.

### 3.5. Comparison of the catalyst activities

Table 4 shows the comparison of the previous methods (entries 1–10) used for the synthesis of a(1–12) with our proposed method (entry 11). As can be seen, our proposed method has a short time (5 min) with about 90% yield.

### 3.6. Proposed mechanism

Scheme 3 shows the possible mechanism for the synthesis of a(1–12) by E.<sup>43,44</sup>

### 3.7. Recyclability of E

The recovery ability of the E was investigated in the model reaction after four consecutive runs (Fig. 9). At the end of the reaction, E was washed with water and ethanol, dried at 80 °C,



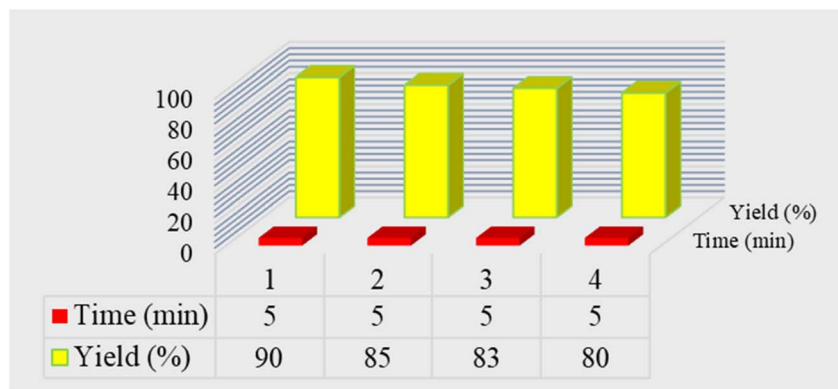


Fig. 9 Recyclability test of E.

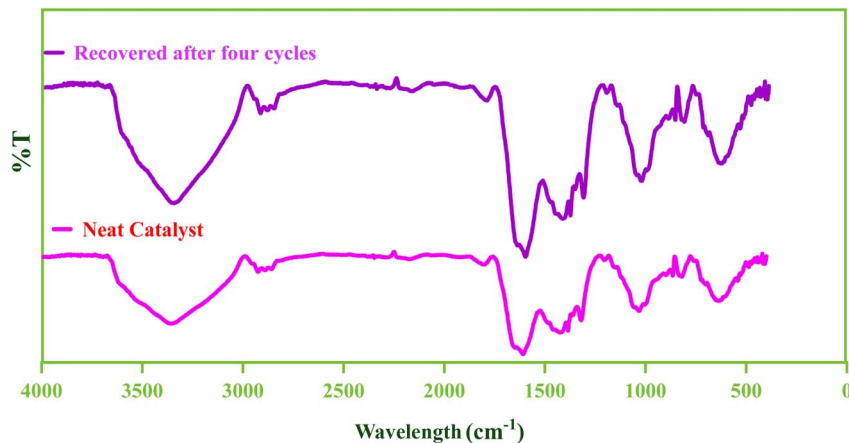


Fig. 10 The FT-IR spectra of the fresh and the used E.

and reused in the next runs. As a result, no significant loss of activity was observed.

In addition, the FT-IR spectrum of E before and after the consecutive runs of recovery showed a very nice similarity (Fig. 10).

## 4. Conclusion

In this study, for the first time, TA oligomers were used as a green ligand for the synthesis of MOFs to modify the surface of the Ce–Mn–LDH. These oligomers have many active sites for chelation with metal by creating metal–phenol–coordinated polymers. Also, FT-IR, ICP, XRD, BET, EDX, SEM, SEM-mapping, TEM, and TGA-DTA techniques showed that the LDH is a suitable surface for the growth of TA oligomers and the formation of metal–organic framework crystals. The catalytic performance of this composite E was evaluated in the synthesis of tetrazolo[1,5-*a*]quinazolines. The high yield of products in a short time and the ability to recycle without side products are the advantages of this composite E.

## Data availability

All data generated or analyzed during this study are included in the ESI.†

## Conflicts of interest

The authors declare that they have no known competing financial interests or personal relationships that could have appeared to influence the work reported in this paper.

## Acknowledgements

The support by the Bu-Ali Sina University is gratefully acknowledged.

## References

- 1 J. Qiu, P. H. Camargo, U. Jeong and Y. Xia, Synthesis, transformation, and utilization of monodispersed colloidal spheres, *Acc. Chem. Res.*, 2019, **52**, 3475–3487.
- 2 P. P. Ghimire and M. Jaroniec, Renaissance of Stöber method for synthesis of colloidal particles: new developments and opportunities, *J. Colloid Interface Sci.*, 2021, **584**, 838–865.
- 3 J. Wei, G. Wang, F. Chen, M. Bai, Y. Liang, H. Wang, D. Zhao and Y. Zhao, Sol-gel synthesis of metal–phenolic coordination spheres and their derived carbon composites, *Angew. Chem., Int. Ed.*, 2018, **57**, 9838–9843.



4 G. Liang, B. Feng, G. Wang, N. Wu, Y. Deng, A. A. Elzatahry, A. Alghamdi, Y. Zhao and J. Wei, Facile synthesis of metal-polyphenol-formaldehyde coordination polymer colloidal nanoparticles with sub-50 nm for T1-weighted magnetic resonance imaging, *Chin. Chem. Lett.*, 2021, **32**, 842–848.

5 H. J. Lee, Y. J. Cho, W. Cho and M. Oh, Controlled isotropic or anisotropic nanoscale growth of coordination polymers: formation of hybrid coordination polymer particles, *ACS Nano*, 2013, **7**, 491–499.

6 H. Huang, J. Qin, G. Wang, Z. Guo, X. Yu, Y. Zhao and J. Wei, Synthesis of spiny metal-phenolic coordination crystals as a sensing platform for sequence-specific detection of nucleic acids, *CrystEngComm*, 2018, **20**, 7626–7630.

7 J. Qin, N. Guo, J. Yang and Y. Chen, Recent advances of metal-polyphenol coordination polymers for biomedical applications, *Biosensors*, 2023, **13**, 776.

8 N. Aelen, M. I. Popa, O. Nova, G. Lisa and L. Balait, Tannic acid incorporation in chitosan-based microparticles and in vitro controlled release, *J. Mater. Sci.: Mater. Med.*, 2009, **20**, 1095–1102.

9 M. A. Gwa, B. M. Hong, J. M. Seok, S. A. Park and W. H. Park, Effect of tannic acid on the mechanical and adhesive properties of catechol-modified hyaluronic acid hydrogels, *Int. J. Biol. Macromol.*, 2021, **191**, 699–705.

10 B. Kaczmarek, Tannic acid with antiviral and antibacterial activity as a promising component of biomaterials-A minireview, *Materials*, 2020, **13**, 3224.

11 Q. Huang, J. Zhao, M. Liu, J. Chen, X. Zhu, T. Wu, J. Tian, Y. Wen, X. Zhang and Y. Wei, Preparation of polyethylene polyamine@tannic acid encapsulated MgAl-layered double hydroxide for the efficient removal of copper(II) ions from aqueous solution, *J. Taiwan Inst. Chem. Eng.*, 2018, **82**, 92–101.

12 L. G. Bach, M. R. Islam, X. T. Cao, J. M. Park and K. T. Lim, A novel photoluminescent nanohybrid of poly( $\varepsilon$ -caprolactone) grafted Mg/Al layered double hydroxides and Tb<sup>3+</sup> ions: synthesis and characterization, *J. Alloys Compd.*, 2014, **582**, 22–28.

13 R. Dou, J. Ma, D. Huang, C. Fan, W. Zhao, M. Peng and S. Komarneni, Bisulfite assisted photocatalytic degradation of methylene blue by Ni-Fe-Mn oxide from MnO<sub>4</sub> intercalated LDH, *Appl. Clay Sci.*, 2018, **161**, 235–241.

14 S. Javadi and D. Habibi, The new sulfonic-acid-based Ce-Mn-layered double hydroxide as a capable nano-catalyst for the green-synthesis of spiro[indoline-pyran] ones and spiro[acenaphthylene-pyran]ones, *Res. Chem. Intermed.*, 2023, **49**, 2005–2024.

15 Y. Yang, X. Yan, X. Hu, R. Feng and M. Zhou, In-situ growth of ZIF-8 on layered double hydroxide: effect of Zn/Al molar ratios on their structural, morphological, and adsorption properties, *J. Colloid Interface Sci.*, 2017, **505**, 206–212.

16 W. D. Zhang, Q. T. Hu, L. L. Wang, J. Gao, H. Y. Zhu, X. Yan and Z. G. Gu, In-situ generated Ni-MOF/LDH heterostructures with abundant phase interfaces for enhanced oxygen evolution reaction, *Appl. Catal., B*, 2021, **286**, 119906.

17 S. Chongd, S. Bhattacharje, P. Bhanj and A. Bhaumi, Porous organic-inorganic hybrid materials for catalysis, energy and environmental applications, *Chem. Commun.*, 2022, **58**, 3429–3460.

18 R. Soltani, R. Pelalak, M. Pishnamazi, A. Marjani, S. M. Sarkar, A. B. Albadarin and S. Shirazian, Novel bimodal micro-mesoporous Ni<sub>50</sub>Co<sub>50</sub>-LDH/UiO-66-NH<sub>2</sub> nano-composite for Tl(I) adsorption, *Arabian J. Chem.*, 2021, **14**, 103058.

19 R. Soltani, R. Pelalak, M. Pishnamazi, A. Marjani and S. Shirazian, A water-stable functionalized NiCo-LDH/MOF nanocomposite: green synthesis, characterization, and its environmental application for heavy metals adsorption, *Arabian J. Chem.*, 2021, **14**, 103052.

20 S. Mallakpour, Z. Radfar and M. Feiz, Chitosan/tannic acid/ZnFe layered double hydroxides and mixed metal oxides nanocomposite for the adsorption of reactive dyes, *Carbohydr. Polym.*, 2023, **305**, 120528.

21 P. R. Patel, H. Joshi, U. Shah, Ma. Bapna and B. Patel, New generation of quinazolinone derivatives as potent antimicrobial agents, *Asian Pacific Journal of Health Sciences*, 2021, **8**, 61–66.

22 M. Asif, Chemical characteristics, synthetic methods, and biological potential of quinazoline and quinazolinone derivatives, *Int. J. Med. Chem.*, 2014, **27**, 395637.

23 J. Devasi, A. Nizam and V. L. Vasanth, Azole-based antibacterial agents: a review on multistep synthesis strategies and biology, *Polycyclic Aromat. Compd.*, 2022, **42**(8), 5474–5495.

24 L. M. Antypen, S. I. Kovalenk, O. M. Antypen, A. M. Kats and O. M. Achkas, Design and evaluation of novel antimicrobial and anticancer agents among tetrazolo[1,5-c] quinazoline-5-thione S-derivatives, *Sci. Pharm.*, 2013, **81**, 15–42.

25 A. Maleki, M. Aghaei and T. Kari, Facile synthesis of 7-arylbenzo[*h*]tetrazolo[5,1-*b*]-quinazoline-5,6-dione fused polycyclic compounds by using a novel magnetic polyurethane catalyst, *Polycyclic Aromat. Compd.*, 2019, **39**, 266–278.

26 L. Wu, Synthesis and biological evaluation of novel 1,2-naphthoquinones possessing tetrazolo[1,5-*a*]pyrimidine scaffolds as potent antitumor agents, *RSC Adv.*, 2015, **5**, 24960–24965.

27 A. Hassankhani, B. Gholipour, S. Rostamni, E. Zarenezhha, N. Nouruz, T. Kavetsky, R. Khalilo and M. Shokouhimeh, Sustainable design and novel synthesis of highly recyclable magnetic carbon containing aromatic sulfonic acid: Fe<sub>3</sub>O<sub>4</sub>@C/Ph-SO<sub>3</sub>H as green solid acid promoted regioselective synthesis of tetrazoloquinazolines, *Appl. Organomet. Chem.*, 2021, **35**, e6346.

28 S. Shen, H. Zhang, C. Yu, C. Yao, T. Li, B. Qin, J. Lu and D. Wang, Solvent-free combinatorial synthesis of tetrazolo[1,5-*a*]thiopyrano[3,4-*d*]pyrimidine derivatives, *Res. Chem. Intermed.*, 2013, **39**, 1799–1806.

29 P. Kour, V. P. Singh, B. Khajuria, T. Singh and A. Kumar, Al(III) chloride catalyzed multi-component domino strategy: synthesis of library of dihydrotetrazolo[1,5-*a*]



pyrimidines and tetrahydrotetrazolo[1,5-*a*]quinazolinones, *Tetrahedron Lett.*, 2017, **58**, 4179–4185.

30 F. Bonyasi, M. Hekmati and H. Veisi, Preparation of core/shell nanostructure  $\text{Fe}_3\text{O}_4@\text{PEG400-SO}_3\text{H}$  as heterogeneous and magnetically recyclable nanocatalyst for one-pot synthesis of substituted pyrroles by Paal-Knorr reaction at room temperature, *J. Colloid Interface Sci.*, 2017, **496**, 177–187.

31 R. Jia, C. Zhao, Z. Huang, X. Liu, D. Wang, Z. Hui and X. Xu, An in-situ growth strategy of NiCo-MOF nanosheets with more activity sites for asymmetric supercapacitors, *Ionics*, 2020, **26**, 6309–6318.

32 X. Tao, Y. Han, C. Sun, L. Huang and D. Xu, Plasma modification of NiAlCe-LDH as improved photocatalyst for organic dye wastewater degradation, *Appl. Clay Sci.*, 2019, **172**, 75–79.

33 Y. Wang, X. Liu, N. Zhang, G. Qiu and R. Ma, Cobalt-doped Ni-Mn layered double hydroxide nanoplates as high-performance electrocatalyst for oxygen evolution reaction, *Appl. Clay Sci.*, 2018, **165**, 277–283.

34 T. Zhang, Z. C. Liu, Y. C. Ye, Y. Wang, H. Q. Yang, H. X. Gao and W. M. Yang, Dry reforming of ethane over FeNi/Al-Ce-O catalysts: composition-induced strong metal-support interactions, *Engineering*, 2022, 173–185.

35 A. N. Wagassa, L. T. Tufa, J. Lee, E. A. Zereffa and T. A. Shifa, Controllable doping of Mn into  $\text{Ni}_{0.075-x}\text{Mn}_x\text{Al}_{0.025}(\text{OH})_2(\text{CO}_3)_{0.0125}\cdot y\text{H}_2\text{O}$  for efficient adsorption of fluoride ions, *Global Challenges*, 2023, **7**, 2300018.

36 M. Wang, X. Yao, Y. Chen, B. Lin, N. Li, K. Zhi, Q. Liu and H. Zhou, A novel tannic acid-based carbon-supported cobalt catalyst for transfer hydrogenation of biomass derived ethyl levulinate, *Front. Chem.*, 2022, **10**, 964128.

37 L. Y. Zeng and C. Cai, Iodine catalyzed one-pot multicomponent synthesis of a library of compounds containing tetrazolo[1,5-*a*]pyrimidine core, *J. Comb. Chem.*, 2010, **12**, 35–40.

38 M. Farahi, B. Karami, A. Jokar and K. Eskandari, An environmentally benign synthesis of pyrimidine-fused coumarin and triazole motifs via a catalytic domino reaction, *Org. Prep. Proced. Int.*, 2017, **49**, 514–524.

39 C. Zhang and W. Li, Regioselective synthesis of 6-aryl-benzo[*h*][1,2,4]-triazolo[5,1-*b*]quinazoline-7,8-diones as potent antitumoral agents, *Bioorg. Med. Chem. Lett.*, 2013, **23**, 5002–5005.

40 A. Hassankhani, B. Gholipour and S. Rostamni, An efficient regioselective three-component synthesis of tetrazoloquinazolines using  $\text{g-C}_3\text{N}_4$  covalently bonded sulfamic acid, *Polyhedron*, 2020, **175**, 114217.

41 A. Hassankhani and E. Mosaddegh, An efficient synthesis of tetrahydrotetrazolo[1,5-*a*]quinazoline derivatives by a three-component reaction of 5-aminotetrazole, aryl-aldehydes, and dimedone, *Sci. Iran.*, 2015, **22**, 942–947.

42 R. Ghorbani-Vaghei, S. Alavinia and N. Sarmast,  $\text{Fe}_3\text{O}_4@\text{SiO}_2@\text{propyl-ANDSA}$ : a new catalyst for the synthesis of tetrazoloquinazolines, *Appl. Organomet. Chem.*, 2018, **32**, e4038.

43 C. Raju, K. Madhaiyan, R. Uma, R. Sridhar and S. Ramakrishna, Antimicrobial and anti-oxidant activity evaluation of tetrazolo[1,5-*a*]pyrimidines: a simple diisopropyl-ammonium trifluoroacetate mediated synthesis, *RSC Adv.*, 2012, **2**, 11657.

44 M. V. Murlykina, A. D. Morozova, I. M. Zviagin, Y. I. Sakhno, S. M. Desenko and V. A. Chebanov, Aminoazole-based diversity-oriented synthesis of heterocycles, *Front. Chem.*, 2018, **6**, 527.

45 S. Akrami, B. Karami and M. Farahi, A new and green approach for regiospecific synthesis of novel chromeno-triazolopyrimidin using tungstic acid immobilized MCM-41 as a reusable catalyst, *J. Heterocycl. Chem.*, 2020, **57**, 2446–2454.

